Search for New Heavy Particles Decaying to $ZZ \to \ell\ell\ell\ell, \ell\ell jj$ in $p\bar{p}$ Collisions at $\sqrt{s} = 1.96$ TeV

T. Aaltonen,[21] B. Álvarez González[v],[9] S. Amerio,[41] D. Amidei,[32] A. Anastassov,[36] A. Annovi,[17] J. Antos,[12] G. Apollinari,[15] J.A. Appel,[15] A. Apresyan,[46] T. Arisawa,[56] A. Artikov,[13] J. Asaadi,[51] W. Ashmanskas,[15] B. Auerbach,[59] A. Aurisano,[51] F. Azfar,[40] W. Badgett,[15] A. Barbaro-Galtieri,[26] V.E. Barnes,[46] B.A. Barnett,[23] P. Barria[cc],[44] P. Bartos,[12] M. Bauce[aa],[41] G. Bauer,[30] F. Bedeschi,[44] D. Beecher,[28] S. Behari,[23] G. Bellettini[bb],[44] J. Bellinger,[58] D. Benjamin,[14] A. Beretvas,[15] A. Bhatti,[48] M. Binkley*,[15] D. Bisello[aa],[41] I. Bizjak[gg],[28] K.R. Bland,[5] B. Blumenfeld,[23] A. Bocci,[14] A. Bodek,[47] D. Bortoletto,[46] J. Boudreau,[45] A. Boveia,[11] B. Brau[a],[15] L. Brigliadori[z],[6] A. Brisuda,[12] C. Bromberg,[33] E. Brucken,[21] M. Bucciantonio[bb],[44] J. Budagov,[13] H.S. Budd,[47] S. Budd,[22] K. Burkett,[15] G. Busetto[aa],[41] P. Bussey,[19] A. Buzatu,[31] C. Calancha,[29] S. Camarda,[4] M. Campanelli,[33] M. Campbell,[32] F. Canelli[12],[15] A. Canepa,[43] B. Carls,[22] D. Carlsmith,[58] R. Carosi,[44] S. Carrillo[k],[16] S. Carron,[15] B. Casal,[9] M. Casarsa,[15] A. Castro[z],[6] P. Catastini,[15] D. Cauz,[52] V. Cavaliere[cc],[44] M. Cavalli-Sforza,[4] A. Cerri[f],[26] L. Cerrito[q],[28] Y.C. Chen,[1] M. Chertok,[7] G. Chiarelli,[44] G. Chlachidze,[15] F. Chlebana,[15] K. Cho,[25] D. Chokheli,[13] J.P. Chou,[20] W.H. Chung,[58] Y.S. Chung,[47] C.I. Ciobanu,[42] M.A. Ciocci[cc],[44] A. Clark,[18] G. Compostella[aa],[41] M.E. Convery,[15] J. Conway,[7] M.Corbo,[42] M. Cordelli,[17] C.A. Cox,[7] D.J. Cox,[7] F. Crescioli[bb],[44] C. Cuenca Almenar,[59] J. Cuevas[v],[9] R. Culbertson,[15] D. Dagenhart,[15] N. d'Ascenzo[t],[42] M. Datta,[15] P. de Barbaro,[47] S. De Cecco,[49] G. De Lorenzo,[4] M. Dell'Orso[bb],[44] C. Deluca,[4] L. Demortier,[48] J. Deng[c],[14] M. Deninno,[6] F. Devoto,[21] M. d'Errico[aa],[41] A. Di Canto[bb],[44] B. Di Ruzza,[44] J.R. Dittmann,[5] M. D'Onofrio,[27] S. Donati[bb],[44] P. Dong,[15] M. Dorigo,[52] T. Dorigo,[41] K. Ebina,[56] A. Elagin,[51] A. Eppig,[32] R. Erbacher,[7] D. Errede,[22] S. Errede,[22] N. Ershaidat[y],[42] R. Eusebi,[51] H.C. Fang,[26] S. Farrington,[40] M. Feindt,[24] J.P. Fernandez,[29] C. Ferrazza[dd],[44] R. Field,[16] G. Flanagan[r],[46] R. Forrest,[7] M.J. Frank,[5] M. Franklin,[20] J.C. Freeman,[15] Y. Funakoshi,[56] I. Furic,[16] M. Gallinaro,[48] J. Galyardt,[10] J.E. Garcia,[18] A.F. Garfinkel,[46] P. Garosi[cc],[44] H. Gerberich,[22] E. Gerchtein,[15] S. Giagu[ee],[49] V. Giakoumopoulou,[3] P. Giannetti,[44] K. Gibson,[45] C.M. Ginsburg,[15] N. Giokaris,[3] P. Giromini,[17] M. Giunta,[44] G. Giurgiu,[23] V. Glagolev,[13] D. Glenzinski,[15] M. Gold,[35] D. Goldin,[51] N. Goldschmidt,[16] A. Golossanov,[15] G. Gomez,[9] G. Gomez-Ceballos,[30] M. Goncharov,[30] O. González,[29] I. Gorelov,[35] A.T. Goshaw,[14] K. Goulianos,[48] A. Gresele,[41] S. Grinstein,[4] C. Grosso-Pilcher,[11] R.C. Group,[55] J. Guimaraes da Costa,[20] Z. Gunay-Unalan,[33] C. Haber,[26] S.R. Hahn,[15] E. Halkiadakis,[50] A. Hamaguchi,[39] J.Y. Han,[47] F. Happacher,[17] K. Hara,[53] D. Hare,[50] M. Hare,[54] R.F. Harr,[57] K. Hatakeyama,[5] C. Hays,[40] M. Heck,[24] J. Heinrich,[43] M. Herndon,[58] S. Hewamanage,[5] D. Hidas,[50] A. Hocker,[15] W. Hopkins[g],[15] D. Horn,[24] S. Hou,[1] R.E. Hughes,[37] M. Hurwitz,[11] U. Husemann,[59] N. Hussain,[31] M. Hussein,[33] J. Huston,[33] G. Introzzi,[44] M. Iori[ee],[49] A. Ivanov[o],[7] E. James,[15] D. Jang,[10] B. Jayatilaka,[14] E.J. Jeon,[25] M.K. Jha,[6] S. Jindariani,[15] W. Johnson,[7] M. Jones,[46] K.K. Joo,[25] S.Y. Jun,[10] T.R. Junk,[15] T. Kamon,[51] P.E. Karchin,[57] Y. Kato[n],[39] W. Ketchum,[11] J. Keung,[43] V. Khotilovich,[51] B. Kilminster,[15] D.H. Kim,[25] H.S. Kim,[25] H.W. Kim,[25] J.E. Kim,[25] M.J. Kim,[17] S.B. Kim,[25] S.H. Kim,[53] Y.K. Kim,[11] N. Kimura,[56] M. Kirby,[15] S. Klimenko,[16] K. Kondo,[56] D.J. Kong,[25] J. Konigsberg,[16] A.V. Kotwal,[14] M. Kreps,[24] J. Kroll,[43] D. Krop,[11] N. Krumnack[l],[5] M. Kruse,[14] V. Krutelyov[d],[51] T. Kuhr,[24] M. Kurata,[53] S. Kwang,[11] A.T. Laasanen,[46] S. Lami,[44] S. Lammel,[15] M. Lancaster,[28] R.L. Lander,[7] K. Lannon[u],[37] A. Lath,[50] G. Latino[cc],[44] I. Lazzizzera,[41] T. LeCompte,[2] E. Lee,[51] H.S. Lee,[11] J.S. Lee,[25] S.W. Lee[w],[51]

S. Leo[bb],[44] S. Leone,[44] J.D. Lewis,[15] C.-J. Lin,[26] J. Linacre,[40] M. Lindgren,[15] E. Lipeles,[43] A. Lister,[18] D.O. Litvintsev,[15] C. Liu,[45] Q. Liu,[46] T. Liu,[15] S. Lockwitz,[59] N.S. Lockyer,[43] A. Loginov,[59] D. Lucchesi[aa],[41] J. Lueck,[24] P. Lujan,[26] P. Lukens,[15] G. Lungu,[48] J. Lys,[26] R. Lysak,[12] R. Madrak,[15] K. Maeshima,[15] K. Makhoul,[30] P. Maksimovic,[23] S. Malik,[48] G. Manca[b],[27] A. Manousakis-Katsikakis,[3] F. Margaroli,[46] C. Marino,[24] M. Martínez,[4] R. Martínez-Ballarín,[29] P. Mastrandrea,[49] M. Mathis,[23] M.E. Mattson,[57] P. Mazzanti,[6] K.S. McFarland,[47] P. McIntyre,[51] R. McNulty[i],[27] A. Mehta,[27] P. Mehtala,[21] A. Menzione,[44] C. Mesropian,[48] T. Miao,[15] D. Mietlicki,[32] A. Mitra,[1] H. Miyake,[53] S. Moed,[20] N. Moggi,[6] M.N. Mondragon[k],[15] C.S. Moon,[25] R. Moore,[15] M.J. Morello,[15] J. Morlock,[24] P. Movilla Fernandez,[15] A. Mukherjee,[15] Th. Muller,[24] P. Murat,[15] M. Mussini[z],[6] J. Nachtman[m],[15] Y. Nagai,[53] J. Naganoma,[56] I. Nakano,[38] A. Napier,[54] J. Nett,[51] C. Neu,[55] M.S. Neubauer,[22] J. Nielsen[e],[26] L. Nodulman,[2] O. Norniella,[22] E. Nurse,[28] L. Oakes,[40] S.H. Oh,[14] Y.D. Oh,[25] I. Oksuzian,[55] T. Okusawa,[39] R. Orava,[21] L. Ortolan,[4] S. Pagan Griso[aa],[41] C. Pagliarone,[52] E. Palencia[f],[9] V. Papadimitriou,[15] A.A. Paramonov,[2] J. Patrick,[15] G. Pauletta[ff],[52] M. Paulini,[10] C. Paus,[30] D.E. Pellett,[7] A. Penzo,[52] T.J. Phillips,[14] G. Piacentino,[44] E. Pianori,[43] J. Pilot,[37] K. Pitts,[22] C. Plager,[8] L. Pondrom,[58] K. Potamianos,[46] O. Poukhov*,[13] F. Prokoshin[x],[13] A. Pronko,[15] F. Ptohos[h],[17] E. Pueschel,[10] G. Punzi[bb],[44] J. Pursley,[58] A. Rahaman,[45] V. Ramakrishnan,[58] N. Ranjan,[46] I. Redondo,[29] P. Renton,[40] M. Rescigno,[49] F. Rimondi[z],[6] L. Ristori[45],[15] A. Robson,[19] T. Rodrigo,[9] T. Rodriguez,[43] E. Rogers,[22] S. Rolli,[54] R. Roser,[15] M. Rossi,[52] F. Rubbo,[15] F. Ruffini[cc],[44] A. Ruiz,[9] J. Russ,[10] V. Rusu,[15] A. Safonov,[51] W.K. Sakumoto,[47] Y. Sakurai,[56] L. Santi[ff],[52] L. Sartori,[44] K. Sato,[53] V. Saveliev[t],[42] A. Savoy-Navarro,[42] P. Schlabach,[15] A. Schmidt,[24] E.E. Schmidt,[15] M.P. Schmidt*,[59] M. Schmitt,[36] T. Schwarz,[7] L. Scodellaro,[9] A. Scribano[cc],[44] F. Scuri,[44] A. Sedov,[46] S. Seidel,[35] Y. Seiya,[39] A. Semenov,[13] F. Sforza[bb],[44] A. Sfyrla,[22] S.Z. Shalhout,[7] T. Shears,[27] P.F. Shepard,[45] M. Shimojima[s],[53] S. Shiraishi,[11] M. Shochet,[11] I. Shreyber,[34] A. Simonenko,[13] P. Sinervo,[31] A. Sissakian*,[13] K. Sliwa,[54] J.R. Smith,[7] F.D. Snider,[15] A. Soha,[15] S. Somalwar,[50] V. Sorin,[4] P. Squillacioti,[15] M. Stancari,[15] M. Stanitzki,[59] R. St. Denis,[19] B. Stelzer,[31] O. Stelzer-Chilton,[31] D. Stentz,[36] J. Strologas,[35] G.L. Strycker,[32] D. Stuart[d],[15] Y. Sudo,[53] A. Sukhanov,[16] I. Suslov,[13] K. Takemasa,[53] Y. Takeuchi,[53] J. Tang,[11] M. Tecchio,[32] P.K. Teng,[1] J. Thom[g],[15] J. Thome,[10] G.A. Thompson,[22] E. Thomson,[43] P. Ttito-Guzmán,[29] S. Tkaczyk,[15] D. Toback,[51] S. Tokar,[12] K. Tollefson,[33] T. Tomura,[53] D. Tonelli,[15] S. Torre,[17] D. Torretta,[15] P. Totaro[ff],[52] M. Trovato[dd],[44] Y. Tu,[43] F. Ukegawa,[53] S. Uozumi,[25] A. Varganov,[32] F. Vázquez[k],[16] G. Velev,[15] C. Vellidis,[3] M. Vidal,[29] I. Vila,[9] R. Vilar,[9] J. Vizán,[9] M. Vogel,[35] G. Volpi[bb],[44] P. Wagner,[43] R.L. Wagner,[15] T. Wakisaka,[39] R. Wallny,[8] S.M. Wang,[1] A. Warburton,[31] D. Waters,[28] M. Weinberger,[51] W.C. Wester III,[15] B. Whitehouse,[54] D. Whiteson[c],[43] A.B. Wicklund,[2] E. Wicklund,[15] S. Wilbur,[11] F. Wick,[24] H.H. Williams,[43] J.S. Wilson,[37] P. Wilson,[15] B.L. Winer,[37] P. Wittich[g],[15] S. Wolbers,[15] H. Wolfe,[37] T. Wright,[32] X. Wu,[18] Z. Wu,[5] K. Yamamoto,[39] J. Yamaoka,[14] T. Yang,[15] U.K. Yang[p],[11] Y.C. Yang,[25] W.-M. Yao,[26] G.P. Yeh,[15] K. Yi[m],[15] J. Yoh,[15] K. Yorita,[56] T. Yoshida[j],[39] G.B. Yu,[14] I. Yu,[25] S.S. Yu,[15] J.C. Yun,[15] A. Zanetti,[52] Y. Zeng,[14] and S. Zucchelli[z6]

(CDF Collaboration[†])

[1]*Institute of Physics, Academia Sinica, Taipei, Taiwan 11529, Republic of China*
[2]*Argonne National Laboratory, Argonne, Illinois 60439, USA*
[3]*University of Athens, 157 71 Athens, Greece*
[4]*Institut de Fisica d'Altes Energies, ICREA, Universitat Autonoma de Barcelona, E-08193, Bellaterra (Barcelona), Spain*
[5]*Baylor University, Waco, Texas 76798, USA*
[6]*Istituto Nazionale di Fisica Nucleare Bologna,*
[z]*University of Bologna, I-40127 Bologna, Italy*
[7]*University of California, Davis, Davis, California 95616, USA*
[8]*University of California, Los Angeles, Los Angeles, California 90024, USA*
[9]*Instituto de Fisica de Cantabria, CSIC-University of Cantabria, 39005 Santander, Spain*
[10]*Carnegie Mellon University, Pittsburgh, Pennsylvania 15213, USA*

[11]Enrico Fermi Institute, University of Chicago, Chicago, Illinois 60637, USA
[12]Comenius University, 842 48 Bratislava,
Slovakia; Institute of Experimental Physics, 040 01 Kosice, Slovakia
[13]Joint Institute for Nuclear Research, RU-141980 Dubna, Russia
[14]Duke University, Durham, North Carolina 27708, USA
[15]Fermi National Accelerator Laboratory, Batavia, Illinois 60510, USA
[16]University of Florida, Gainesville, Florida 32611, USA
[17]Laboratori Nazionali di Frascati, Istituto Nazionale di Fisica Nucleare, I-00044 Frascati, Italy
[18]University of Geneva, CH-1211 Geneva 4, Switzerland
[19]Glasgow University, Glasgow G12 8QQ, United Kingdom
[20]Harvard University, Cambridge, Massachusetts 02138, USA
[21]Division of High Energy Physics, Department of Physics,
University of Helsinki and Helsinki Institute of Physics, FIN-00014, Helsinki, Finland
[22]University of Illinois, Urbana, Illinois 61801, USA
[23]The Johns Hopkins University, Baltimore, Maryland 21218, USA
[24]Institut für Experimentelle Kernphysik, Karlsruhe Institute of Technology, D-76131 Karlsruhe, Germany
[25]Center for High Energy Physics: Kyungpook National University,
Daegu 702-701, Korea; Seoul National University, Seoul 151-742,
Korea; Sungkyunkwan University, Suwon 440-746,
Korea; Korea Institute of Science and Technology Information,
Daejeon 305-806, Korea; Chonnam National University, Gwangju 500-757,
Korea; Chonbuk National University, Jeonju 561-756, Korea
[26]Ernest Orlando Lawrence Berkeley National Laboratory, Berkeley, California 94720, USA
[27]University of Liverpool, Liverpool L69 7ZE, United Kingdom
[28]University College London, London WC1E 6BT, United Kingdom
[29]Centro de Investigaciones Energeticas Medioambientales y Tecnologicas, E-28040 Madrid, Spain
[30]Massachusetts Institute of Technology, Cambridge, Massachusetts 02139, USA
[31]Institute of Particle Physics: McGill University, Montréal,
Québec, Canada H3A 2T8; Simon Fraser University, Burnaby,
British Columbia, Canada V5A 1S6; University of Toronto,
Toronto, Ontario, Canada M5S 1A7; and TRIUMF,
Vancouver, British Columbia, Canada V6T 2A3
[32]University of Michigan, Ann Arbor, Michigan 48109, USA
[33]Michigan State University, East Lansing, Michigan 48824, USA
[34]Institution for Theoretical and Experimental Physics, ITEP, Moscow 117259, Russia
[35]University of New Mexico, Albuquerque, New Mexico 87131, USA
[36]Northwestern University, Evanston, Illinois 60208, USA
[37]The Ohio State University, Columbus, Ohio 43210, USA
[38]Okayama University, Okayama 700-8530, Japan
[39]Osaka City University, Osaka 588, Japan
[40]University of Oxford, Oxford OX1 3RH, United Kingdom
[41]Istituto Nazionale di Fisica Nucleare, Sezione di Padova-Trento,
[aa]University of Padova, I-35131 Padova, Italy
[42]LPNHE, Universite Pierre et Marie Curie/IN2P3-CNRS, UMR7585, Paris, F-75252 France
[43]University of Pennsylvania, Philadelphia, Pennsylvania 19104, USA
[44]Istituto Nazionale di Fisica Nucleare Pisa, [bb]University of Pisa,
[cc]University of Siena and [dd]Scuola Normale Superiore, I-56127 Pisa, Italy
[45]University of Pittsburgh, Pittsburgh, Pennsylvania 15260, USA
[46]Purdue University, West Lafayette, Indiana 47907, USA
[47]University of Rochester, Rochester, New York 14627, USA
[48]The Rockefeller University, New York, New York 10065, USA
[49]Istituto Nazionale di Fisica Nucleare, Sezione di Roma 1,
[ee]Sapienza Università di Roma, I-00185 Roma, Italy
[50]Rutgers University, Piscataway, New Jersey 08855, USA
[51]Texas A&M University, College Station, Texas 77843, USA
[52]Istituto Nazionale di Fisica Nucleare Trieste/Udine,
I-34100 Trieste, [ff]University of Trieste/Udine, I-33100 Udine, Italy
[53]University of Tsukuba, Tsukuba, Ibaraki 305, Japan
[54]Tufts University, Medford, Massachusetts 02155, USA

[55] University of Virginia, Charlottesville, VA 22906, USA
[56] Waseda University, Tokyo 169, Japan
[57] Wayne State University, Detroit, Michigan 48201, USA
[58] University of Wisconsin, Madison, Wisconsin 53706, USA
[59] Yale University, New Haven, Connecticut 06520, USA

We report on a search for anomalous production of Z pairs through a massive resonance decay in data corresponding to 2.5–2.9 fb^{-1} of integrated luminosity in $p\bar{p}$ collisions at $\sqrt{s} = 1.96$ TeV using the CDF II detector at the Fermilab Tevatron. This analysis, with more data and channels where the Z bosons decay to muons or jets, supersedes the 1.1 fb^{-1} four-electron channel result previously published by CDF. In order to maintain high efficiency for muons, we use a new forward tracking algorithm and muon identification requirements optimized for these high signal-to-background channels. Predicting the dominant backgrounds in each channel entirely from sideband data samples, we observe four-body invariant mass spectra above 300 GeV/c^2 that are consistent with background. We set limits using the acceptance for a massive graviton resonance that are 7–20 times stronger than the previously published direct limits on resonant ZZ production.

PACS numbers: 12.60.Cn,13.85.Rm,14.70.Hp

I. INTRODUCTION

The standard model of particle physics (SM) has been enormously successful, but many key questions remain to be answered by a more complete theory. New theoretical ideas can be tested with collider experiments, but it is also worthwhile for experiments to search broadly for anomalous "signatures". One common tactic is to look where experiments are keenly sensitive. The consummate example of this method is the Z' boson search, in which a low-background, well-understood observable (the dilepton invariant mass) is used to constrain the new physics models that happen to predict a dilepton resonance. Diboson resonance searches are an attractive analog of the Z' searches, involving higher multiplicities of the same final states and additional mass constraints, both of which serve to further suppress experimental backgrounds. The irreducible SM diboson background processes occur at such a low rate that they have only recently been observed at the Tevatron [1, 2] at low diboson mass ($M_{ZZ} < 300$ GeV/c^2). At high diboson mass ($M_{ZZ} > 300$ GeV/c^2) the total backgrounds are tiny.

This article presents a search for a diboson resonance in data corresponding to 2.5–2.9 fb^{-1} of integrated luminosity in $\sqrt{s} = 1.96$ TeV $p\bar{p}$ collisions at the CDF II detector at the Fermilab Tevatron, in the decay channel $X \to ZZ$. These ZZ processes have been well-studied at the LEP experiments, which observed no significant deviation from the standard model expectation up to an e^+e^- center-of-mass energy of 207 GeV [3–6]. The LEP data place only indirect constraints on heavier, resonant ZZ production [7], however, and direct production constraints at high ZZ masses must be probed at hadron colliders. To the previously published CDF search for four-electron production via $X \to ZZ \to eeee$ with data corresponding to 1.1 fb^{-1} of integrated luminosity [8], we now add the dijet channels $eejj$ and $\mu\mu jj$, which improve sensitivity at very high X masses where their background is negligible, and the four-electron or -muon channels $ee\mu\mu$

*Deceased
†With visitors from [a]University of Massachusetts Amherst, Amherst, Massachusetts 01003, [b]Istituto Nazionale di Fisica Nucleare, Sezione di Cagliari, 09042 Monserrato (Cagliari), Italy, [c]University of California Irvine, Irvine, CA 92697, [d]University of California Santa Barbara, Santa Barbara, CA 93106 [e]University of California Santa Cruz, Santa Cruz, CA 95064, [f]CERN,CH-1211 Geneva, Switzerland, [g]Cornell University, Ithaca, NY 14853, [h]University of Cyprus, Nicosia CY-1678, Cyprus, [i]University College Dublin, Dublin 4, Ireland, [j]University of Fukui, Fukui City, Fukui Prefecture, Japan 910-0017, [k]Universidad Iberoamericana, Mexico D.F., Mexico, [l]Iowa State University, Ames, IA 50011, [m]University of Iowa, Iowa City, IA 52242, [n]Kinki University, Higashi-Osaka City, Japan 577-8502, [o]Kansas State University, Manhattan, KS 66506, [p]University of Manchester, Manchester M13 9PL, England, [q]Queen Mary, University of London, London, E1 4NS, England, [r]Muons, Inc., Batavia, IL 60510, [s]Nagasaki Institute of Applied Science, Nagasaki, Japan, [t]National Research Nuclear University, Moscow, Russia, [u]University of Notre Dame, Notre Dame, IN 46556, [v]Universidad de Oviedo, E-33007 Oviedo, Spain, [w]Texas Tech University, Lubbock, TX 79609, [x]Universidad Tecnica Federico Santa Maria, 110v Valparaiso, Chile, [y]Yarmouk University, Irbid 211-63, Jordan, [gg]On leave from J. Stefan Institute, Ljubljana, Slovenia,

and $\mu\mu\mu\mu$, which contribute sensitivity to new physics at intermediate masses where the Z + jet(s) backgrounds are larger.

Because there are four or more outgoing leptons or quarks, the analysis is sensitive to single lepton and jet reconstruction efficiencies to approximately the fourth power. In particular, events may often have one or more leptons with $|\eta| > 1$ where muon acceptance and tracking efficiency are lower than for $|\eta| < 1$. Consequently the four-lepton channels motivate development and use of techniques to improve electron and muon reconstruction and identification efficiencies while exploiting the kinematics of the signature to keep backgrounds low. To augment forward muon coverage, the present analysis also employs, for the first time, a new method of reconstructing charged particles in the silicon detectors using constraints from particle traces in forward regions with partial wire tracker coverage.

The aim of the search is sensitivity to any massive particle that could decay to ZZ. Though we avoid focus on any one specific model, we choose a benchmark process that is implemented in several popular Monte Carlo generation programs, the virtual production of gravitons in a simple Randall-Sundrum RS1 scenario [9, 10], to fix acceptance for the search and quantify its sensitivity. The geometry of the model consists of two three-branes separated from each other by a single extra dimension. Boundary conditions at the branes quantize the momentum in the extra dimension, leading to a Kaluza-Klein tower of discrete, massive gravitons. In RS1 scenarios with the standard model particles confined to either brane, a discovery would involve graviton decays directly to photons or leptons—the graviton branching ratio to ZZ is significant but the Z branching ratio to leptons is small. In more complex but well-motivated scenarios with SM particles allowed in the extra dimension, however, graviton decays to photons, leptons, and light jets can be suppressed, and dibosons become an important discovery channel [11, 12].

The organization of this article is as follows: Section 2 describes relevant components of the CDF II detector; Section 3, the event selection; Section 4, the background estimates; and Section 5, the results.

II. THE CDF II DETECTOR

The CDF II detector is a general purpose magnetic spectrometer surrounded by electromagnetic and hadronic calorimeters and muon detectors designed to record Tevatron $p\bar{p}$ collisions. We briefly describe the components of the detector relevant to this search. A complete description can be found elsewhere [13].

A combination of tracking systems reconstructs the trajectories and measures momenta of charged particles in a 1.4 T solenoidal magnetic field. Trajectories of charged particles are reconstructed using an eight-layer silicon microstrip vertex tracker [14] at radii $1.3 < r < 29$ cm from the nominal beamline[1] and a 96-layer open-cell drift chamber (COT) providing eight superlayers of alternating stereo and axial position measurements [15] at large radii $43 < r < 132$ cm. The COT provides full geometric coverage for $|\eta| < 1.0$. The average radius of the lowest radius axial (stereo) COT superlayer is 58 (46) cm, providing partial coverage for $|\eta| < 1.7(1.9)$. The silicon tracker provides full coverage for $|\eta| < 1.8$.

Outside the tracking volume, segmented electromagnetic (EM) lead-scintillator and hadronic (HAD) iron-scintillator sampling calorimeters measure particle energies [16]. The central ($|\eta| < 1.1$) calorimeters are arranged around the interaction point in a projective-tower cylindrical geometry, divided azimuthally into 15° wedges. This calorimeter measures electron energies with a resolution of $[\sigma(E)/E]^2 = (13.5\%)^2/E_T + (2\%)^2$. The forward calorimeters ($1.1 < |\eta| < 3.6$) are arranged in an azimuthally-symmetric disk geometry and measure electron energies with a resolution of $[\sigma(E)/E]^2 = (16.0\%)^2/E + (1\%)^2$. Wire chambers (scintillator strips) embedded in the central (forward) EM calorimeters at $\sim 6X_0$, the average depth of shower maximum, provide position and lateral shower development measurements for $|\eta| < 2.5$.

Beyond the calorimeters, muon drift chambers and scintillators measure particles that traverse

[1] CDF uses a cylindrical coordinate system in which θ (ϕ) is the polar (azimuthal) angle, r is the radius from the nominal beam axis, and $+z$ points along the proton beam direction and is zero at the center of the detector. The pseudorapidity is defined as $\eta \equiv -\ln\tan(\theta/2)$. Energy (momentum) transverse to the beam is defined $E_{\rm T} \equiv E\sin\theta$ ($p_{\rm T} \equiv p\sin\theta$), where E is energy and p is momentum.

the entire inner and outer detectors and reject the instrumental backgrounds of the central muon triggers. The central muon chambers (CMU) lie just outside the central hadronic calorimeter with ϕ-dependent coverage for $0.03 < |\eta| < 0.63$. The central muon upgrade (CMP) augments the CMU coverage in ϕ and lies behind another approximately 3 interaction lengths of steel. The central muon extension (CMX) extends coverage into the region $0.65 < |\eta| < 1.0$.

The beam luminosity is determined by measuring the inelastic $p\bar{p}$ collision rate with gas Cherenkov detectors [17], located in the region $3.7 < |\eta| < 4.7$.

At each bunch crossing, a three-level trigger system [13] scans the detector output for $|\eta| < 1.1$ electrons or $|\eta| < 1.0$ muons with at least 18 GeV/c of transverse momentum. We accept events that satisfy one of four trigger paths: one that requires a deposition of at least 18 GeV transverse energy in the calorimeter consistent with an electron and a matching COT track with at least 9 GeV/c of transverse momentum; another with fewer electron identification requirements intended to ensure high efficiency for very energetic electrons; a muon path requiring a COT track with at least 18 GeV/c of transverse momentum pointing toward signals in both the CMU and CMP chambers (a CMUP trigger) and traversing the calorimeter consistent with a minimum-ionizing particle; or a similar muon path with signals in the CMX chamber instead of the CMU and CMP chambers.

III. DATA COLLECTION

We use data corresponding to an integrated luminosity of 2.5–2.9 fb^{-1} depending on the data quality criteria applicable to the relevant ZZ decay channel. We separately analyze six channels: $eeee$, $ee\mu\mu$, $\mu\mu ee$, $\mu\mu\mu\mu$, $eejj$, and $\mu\mu jj$. Events are divided into the six categories based on the trigger, where the first lepton denotes the required trigger path, and the presence of lepton and jet candidates identified using the criteria listed in Tables I through IV. The trigger lepton criteria are the most stringent; subsequent kinematic signature selections yield very low backgrounds, allowing very efficient identification criteria to be used for the other lepton candidates. Events accepted by either electron trigger path and containing at least one electron candidate that fired the electron trigger and satisfied the offline selection criteria are excluded from the muon-triggered categories. There are no events that satisfy the requirements of more than one category.

TABLE I: Calorimeter electron identification criteria. We require Had/EM, the ratio of energies measured in the hadronic and electromagnetic calorimeters, to be less than $f(E) = 0.055 + 0.00045 \times (E/\text{GeV})$ where E is the measured calorimeter energy. Iso_{cal} is the calorimeter energy measured within $\Delta R = 0.4$ centered on the electron, excluding the electron energy. η_{det} is calculated assuming an origin at $z = 0$. LshrTrk is a lateral shower shape variable described in Ref. [18].

Criteria	Trigger	Central	Forward
E_T(GeV)	> 20	> 5	> 5
$\lvert$Track $z_0\rvert$ (cm)	< 60	< 60	
Had/EM	$< f(E)$	$< f(E)$	< 0.05
$\text{Iso}_{\text{cal}}/E_{\text{cal}}$	< 0.2	< 0.2	< 0.2
$\lvert\eta_{\text{det}}\rvert$			< 2.5
LshrTrk	< 0.4		
Track p_T (GeV/c)	> 10		

During this selection we identify the events containing at least two leptons (including the trigger lepton) using the nominal CDF event reconstruction software. We reprocess these events using a revision of the software with improved tracking, including more efficient forward tracking algorithms, and then select all final states from the reprocessed data. In this way, we avoid CPU-intensive reconstruction of a 96.6% subset of the sample that has no chance to pass our final selection. Nevertheless, two subsets of the data corresponding to 200 pb^{-1} of integrated luminosity each were fully reprocessed without the initial two-lepton selection and analyzed to confirm that the procedure used for the full dataset is fully efficient for events of interest to the analysis.

The electron criteria listed in Tables I through II are nearly identical to the previous $eeee$ analysis [8]. The double Z mass peak signature admits little background, allowing appreciably more efficient electron criteria than those used for many other CDF analyses (for example, Ref. [13]). We require either an isolated calorimeter cluster with electron-like energy deposition or, to recover acceptance, an isolated track pointing at uninstrumented regions of the calorimeters. Such regions constitute approximately 17% of the solid angle

TABLE II: Track electron identification criteria. Tracks must consist of measurements in several COT superlayers. Silicon measurements are not required. $\mathrm{Iso_{trk}}$ is the scalar sum of the momenta of all tracks measured within a circle of $\Delta R = 0.4$ centered on the electron track direction. ΔR_{EM} is the separation in the $\eta - \phi$ plane between the electron track and the nearest calorimeter electron cluster.

Criteria	
p_T (GeV/c)	> 10
Axial Superlayers	> 3
Stereo Superlayers	> 2
$\lvert$Track $z_0\rvert$ (cm)	< 60
p_{trk} / $(\mathrm{Iso_{trk}} + p_{\mathrm{trk}})$	> 0.9
$\lvert d_0 \rvert$	$< \begin{cases} 200\ \mu\mathrm{m} & \text{silicon} \\ 2\ \mathrm{mm} & \text{no silicon} \end{cases}$
ΔR_{EM}	> 0.2

for $|\eta| < 1.2$ and would otherwise reduce our four-electron acceptance by a factor of two. The transverse energy threshold for non-trigger electrons is 5 GeV. As the mass of the signal resonance $X \to ZZ$ increases, the energies of the two Z decay products become asymmetric in the detector frame, and thus our criteria must efficiently select leptons with transverse momentum of order 10 GeV/c as well as leptons with p_{T} of hundreds of GeV/c.

The muon criteria listed in Table III require an isolated track satisfying basic track quality criteria and depositing minimal energy in the calorimeter. We make use of a new track reconstruction algorithm, described in the Appendix, and apply less stringent energy and isolation requirements than typical for CDF high p_{T} analyses so as to increase our acceptance and efficiency. Muon candidate tracks may be matched to information in the muon chambers, but to recover acceptance lost due to gaps in chamber coverage and to recover efficiency lost due to pointing requirements, chamber matching is not required except for the trigger muon.

Jets must satisfy the criteria listed in Table IV and jet energies are corrected for instrumental effects [20]. Before relying on the jet energy measurements for the two-lepton two-jet analysis, we have verified that these corrections balance transverse momentum in the Z + jet(s) events considered here. We choose kinematic requirements on individual jet energies, on dijet invariant masses, and on four-body masses involving jet final states so that the systematic uncertainties on $X \to ZZ$ signal acceptances and efficiencies from mis-modeling of QCD radiation or jet reconstruction effects are small.

TABLE III: Muon identification criteria. The CMU, CMP, and CMX match variables compare the track position extrapolated to the relevant muon chambers with the chamber position measurements. The non-trigger p_T requirement is lower for tracks with muon chamber information attached. $\mathrm{Iso_{trk}}$ is the scalar sum p_{T} of all tracks measured within a circle of $\Delta R = 0.4$ centered on the muon track direction. E_{EM} and E_{HAD} are the electromagnetic and hadronic calorimeter energies recorded in towers intersected by the muon track, and $f_{EM}(p^{trk}) = 4 + \max(0, 0.0115 * (\frac{p^{trk}}{\mathrm{GeV}/c} - 100))$ and $f_{HAD}(p^{trk}) = 12 + \max(0, 0.028 * (\frac{p^{trk}}{\mathrm{GeV}/c} - 100))$ are functions of the track momentum. The cuts on track curvature κ, its uncertainty σ_κ, and the χ^2 probability of the fit $\mathrm{Prob}(\chi^2, n_{\mathrm{dof}})$ reject poorly measured tracks.

Criteria	CMUP	CMX	Non-trigger
p_T^{trk}(GeV/c)	> 20	> 20	$> 2, 10$
CMU match	< 10 cm		
CMP match	< 20 cm		
CMX match		< 10 cm	
	common to all categories		
$\mathrm{Iso}^{\mathrm{cal}}/p^{trk}$	< 0.2		
E_{EM}(GeV)	$< f_{EM}(p^{trk})$		
E_{HAD}(GeV)	$< f_{HAD}(p^{trk})$		
κ/σ_κ	> 2.5		
$\mathrm{Prob}(\chi^2, n_{\mathrm{dof}})$	$> 10^{-10}$		
$\lvert z_0 \rvert (cm)$	< 60		
$\lvert d_0 \rvert$	$< \begin{cases} 200\ \mu\mathrm{m} & \text{silicon} \\ 2\ \mathrm{mm} & \text{no silicon} \end{cases}$		

Figs. 1 and 2 show comparisons of the peaking and background components of the dielectron and dimuon yield. The combination of our changes to the identification criteria and to the tracking algorithms increases the peak yield by factors of 1.8 and 4.3, respectively.

Measurements of the $p\bar{p} \to \gamma^*/Z \to ee$ and $p\bar{p} \to \gamma^*/Z \to \mu\mu$ cross-sections provide an important test of our understanding of the trigger, reconstruction, and identification efficiencies and Monte Carlo modeling for this new lepton selection. We divide the data into 18 data-taking periods and measure each of the above efficiencies for each period. For each period, we then com-

TABLE IV: Jet identification criteria. The JETCLU algorithm is discussed in Ref. [19]. ΔR_{EM} is the separation in the $\eta - \phi$ plane between centroids of the jet cluster and the nearest electron cluster.

Selection Criteria	
Algorithm	JETCLU 0.4 Cone
$E_T^{\rm raw}$(GeV)	> 10
$\lvert\eta_{\rm centroid}\rvert$	< 3.64
E_{EM}/E_{tot}	< 0.95
ΔR_{EM}	> 0.4

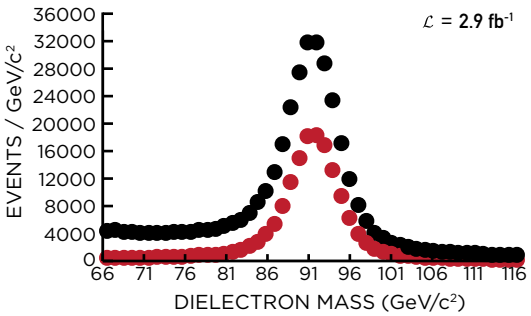

FIG. 1: $Z \to ee$ yield and background comparison between dielectron candidates consisting of a trigger electron and an electron candidate satisfying either (lower set of points) the CDF standard electron criteria or (upper set of points) the criteria employed in the present analysis. The peak yield increases from about 146,000 with the standard criteria to 256,000 candidates with our optimized criteria, while the increase in sideband background is modest.

pute the Drell-Yan cross-section for all combinations of trigger and lepton type using a signal plus background fit to the data and Drell-Yan Monte Carlo. The average instantaneous luminosity tends to increase with data-taking period as Tevatron upgrades were brought online. Figs. 3 and 4 show the resultant cross-sections and their dependence on time.

For the cases where both electron energy measurements come from the calorimeters, the fit signal function is a Breit-Wigner fixed to the world average Z mass and width convolved with a Gaussian resolution function. In the trigger plus track lepton sample, where there is a significant radiative tail below the Z mass, the signal function is a Crystal Ball function. In the combined sample both functions are included. In all cases, the background function is an exponential. The combined result for the electron selection, 249.4 ± 1.6 pb for the mass range $66 < M_{\ell\ell} < 116\,\mathrm{GeV}/c^2$, is in agreement with the dedicated CDF measurement $\sigma_{\gamma^*/Z} \times \mathrm{Br}(p\bar{p} \to \gamma^*/Z \to \ell\ell) = 254.9 \pm 3.3(\mathrm{stat.}) \pm 4.6(\mathrm{sys.})$ [13] and is evidence that the constituent efficiencies

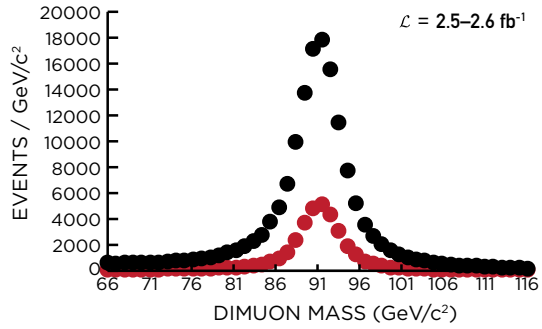

FIG. 2: $Z \to \mu\mu$ yield and background comparison between dimuon candidates consisting of a trigger muon and an muon candidate satisfying either (lower set of points) the CDF standard muon criteria or (upper set of points) the criteria employed in the present analysis. The peak yield increases from about 35,000 candidates with the standard criteria and tracking to 150,000 candidates with our optimized criteria and tracking.

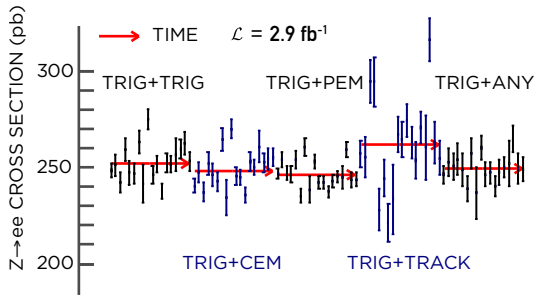

FIG. 3: $Z \to ee$ cross-sections (and averaged cross-sections) for $66 < M_{\ell\ell} < 116$ GeV/c^2 and various selections. The horizontal axis indicates the 18 periods for five selections in succession: two trigger electrons (252.1 ± 1.2 pb), a trigger electron and a central calorimeter electron (TRIG+CEM, 248 ± 1.1 pb), a trigger electron and a forward calorimeter electron (TRIG+PEM, 246.2 ± 0.9 pb), a trigger electron and a track electron (TRIG+TRACK, 262.1 ± 2.3 pb), and, calculated separately, the combination of a trigger electron and any electron selected using the analysis criteria (249.4 ± 1.6 pb). The averaged cross sections are indicated by horizontal lines. Uncertainties are statistical only with the correlated luminosity uncertainty not shown.

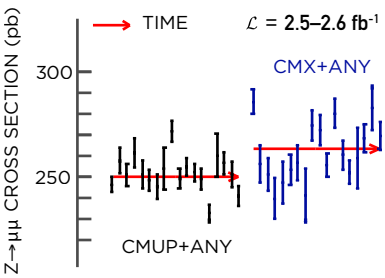

FIG. 4: $Z \to \mu\mu$ cross-sections (and averaged cross-sections) for $66 < M_{\ell\ell} < 116$ GeV/c^2 and various selections. The horizontal axis indicates the 18 periods for two selections in succession: a CMUP trigger muon and another muon satisfying the analysis criteria (250.0 ± 1.2 pb) and a CMX trigger muon combined with another selected muon (263.4 ± 1.8 pb). The averaged cross sections are indicated by horizontal lines. Errors are statistical only with the correlated luminosity uncertainty not shown.

and scale factors are understood well.

Note that there are large variations in the trigger plus track electron cross-section. In these cases, the fit to the data underestimates or overestimates the amount of power-law background contamination of the low dielectron mass radiative tail of the Z. The independent fit to the combination of all selections has a higher signal to noise ratio and is not sensitive to this effect.

The results for the muon selection also show good agreement with the other CDF measurements, except for a 20% shift in the first period and up to a 10% shift in many of the later periods. The origins of the discrepancies have been understood, but not corrected for. Based on these results, we assign a 20% systematic uncertainty on the signal acceptance for each of the six channels. In part because much of the data were collected with the CMUP trigger and during periods with measured cross-sections in good agreement with expectation, this systematic uncertainty over-covers the observed variation and is the dominant uncertainty for the analysis.

IV. KINEMATIC ANALYSIS

After selecting four final states, we consider all possible four-lepton $\ell\ell\ell\ell$ or two-lepton two-jet $\ell\ell jj$ combinations for each event that contains a trigger lepton. No requirement is made on the mass or charge of dilepton pairs. Any two final states must have a minimum separation $\Delta R = \sqrt{\Delta\eta^2 + \Delta\phi^2}$ of 0.2. Dilepton pairs with tracks present for both leptons must point back to the same z_0 production location in order to suppress background from additional pileup interactions. Track timing information is used for a very pure veto of muon and track electron pairs consistent with cosmic rays. There are no events that appear in more than one ZZ decay channel.

For the four-lepton channels, we consider all possible combinations of final states for each event and select the one that minimizes a χ^2 variable quantifying consistency between the dilepton masses and the Z pole mass:

$$\chi^2_{ZZ} = \sum_{i=1,2} \frac{(M_Z^{(i)} - 91.187\,\mathrm{GeV}/c^2)^2}{\sigma^2_{M^{(i)}} + \sigma^2_\Gamma},$$

where $\sigma_{M^{(i)}}$ is the detector mass resolution computed from the individual lepton calorimeter or tracking measurements for the dilepton mass $M_Z^{(i)}$ and a Gaussian approximation with $\sigma_\Gamma = 3.25\,\mathrm{GeV}/c^2$ allows for the nonzero width of the Z resonance.

For the $\ell\ell jj$ channels, we consider all possible combinations of final states and select the two highest E_T jets and the dilepton pairing that minimizes the first term of the equation above. This explicitly avoids possible Z mass bias in the dijet mass spectrum that would complicate the background estimate discussed in the following section. We then require $M_Z > 20\,\mathrm{GeV}/c^2$ for each pairing and, for the dijet channels, $\chi^2_Z < 25$ for the leptonic Z.

A priori we define our signal region to be $M_X > 300\,\mathrm{GeV}/c^2$ so as to avoid most standard model backgrounds. For the $\ell\ell\ell\ell$ modes we further require $\chi^2_{ZZ} < 50$ and for the $\ell\ell jj$ modes we require $65 < M_{jj} < 120\,\mathrm{GeV}/c^2$. Each event may contain additional leptons, jets, or other final states beyond the four that contribute to the signal candidate.

V. BACKGROUND ESTIMATES

For both the four-lepton and the dijet channels, the dominant backgrounds at high M_X are a mixture of Z + jets, $W^\pm$ + jets, multijets, and various lower-rate processes resulting in one or more hadrons that mimic an electron or muon. The diboson processes $W^\pm Z \to jj\ell\ell$, $ZZ \to \ell\ell\ell\ell$, and $ZZ \to \ell\ell jj$ peak at $\chi^2_{ZZ} < 50$ or $65 < M_{jj} < 120\,\mathrm{GeV}/c^2$, while all other back-

grounds do not peak in both Z masses simultaneously. We use a Monte Carlo model to estimate the small contribution from resonant diboson processes and fit sideband data to collectively estimate all backgrounds that do not contain two bosons, collectively referred to as non-resonant background.

We estimate the $\ell\ell\ell\ell$ background by extrapolating the yield in the $185 < M_X < 300\,\mathrm{GeV}/c^2$ region to the signal region ($M_X > 300\,\mathrm{GeV}/c^2$ and $\chi^2_{ZZ} < 50$) using a shape determined from a sample enhanced in non-resonant background. In order to construct samples enriched in this background, four-lepton candidates are selected in which some of the reconstructed leptons are "anti-selected" to fail one or more lepton identification criteria. Anti-selected electrons must fail the HAD/EM energy selection and anti-selected muons must fail the minimum-ionizing energy selection. To further increase available statistics, the isolation requirement is removed for both categories. Events reconstructed with the standard CDF processing that contain at least one trigger lepton and one anti-selected lepton are included in the reprocessing discussed in Section III. The χ^2_{ZZ} vs. M_X distributions for the resultant samples are shown in Figs. 5 and 6.

Figs. 7 and 8 show the invariant mass distributions of trigger lepton plus anti-selected lepton pairings for electrons and muons, respectively. The absence of an appreciable peak indicates few resonant Z events survive the anti-selection.

The two samples of four-body candidates that consist of a trigger lepton and either two- or three-anti-selected leptons with $M_X > 185\,\mathrm{GeV}/c^2$ and $\chi^2_{ZZ} < 500$ are then fit simultaneously to the empirical form

$$f(\chi^2_{ZZ}, M_X) = M_X^{\gamma} \cdot e^{\tau\chi^2_{ZZ}}$$

to determine the falling shape of the $M_{\ell\ell\ell\ell}$ distribution (the power law parameter γ) and the relationship of the number of events in the $\chi^2_{ZZ} < 50$ ZZ window to the number in the off-mass sidebands (the exponential decay parameter τ). As background composition and fake rate kinematic dependence varies with trigger and lepton type, we fit these sidebands separately for the $eeee$, $ee\mu\mu$, $\mu\mu ee$, and $\mu\mu\mu\mu$ background shapes. Figs. 9 through 12 show one-dimensional projections of the fit result for each channel against the fitted two- and three-anti-selected lepton χ^2_{ZZ} and $M_{\ell\ell\ell\ell}$ data as well as the one anti-selected sample, which is not used in the fit. Table V lists the fit parameters obtained with their statistical uncertainty.

TABLE V: Four-lepton background fit results.

Channel	γ	τ
$eeee$	-4.39 ± 0.09	-0.0184 ± 0.0005
$ee\mu\mu$	-5.4 ± 0.2	-0.0161 ± 0.0005
$\mu\mu ee$	-5.3 ± 0.3	-0.020 ± 0.002
$\mu\mu\mu\mu$	-6.5 ± 0.6	-0.030 ± 0.003

TABLE VI: Comparison of non-resonant background mass shape parameter γ fitted independently in the individual sideband samples with the simultaneous fit to the two- and three-anti-selected lepton samples.

Channel	$eeee$	$ee\mu\mu$
Simultaneous	-4.39 ± 0.09	-5.42 ± 0.15
3 anti-leptons	-4.22 ± 0.11	-5.19 ± 0.17
2 anti-leptons	-4.50 ± 0.15	-4.70 ± 0.21
1 anti-lepton	-4.21 ± 0.30	-3.63 ± 0.32
0 anti-leptons	-5.04 ± 0.94	-3.54 ± 0.78
Channel	$\mu\mu ee$	$\mu\mu\mu\mu$
Simultaneous	-5.25 ± 0.34	-6.51 ± 0.61
3 anti-leptons	-4.98 ± 0.50	-6.3 ± 1.1
2 anti-leptons	-4.96 ± 0.41	-6.60 ± 0.73
1 anti-lepton	-5.25 ± 0.73	-5.33 ± 0.92
0 anti-leptons	-5.7 ± 1.6	-4.4 ± 1.3

The background shapes obtained from these fits are normalized so that the sums of the integrals for $185 < M_X < 300\,\mathrm{GeV}/c^2$ and the simulation-derived diboson predictions match the number of events observed with $185 < M_X < 300\,\mathrm{GeV}/c^2$ in the four-lepton samples. The shapes are then extrapolated into the low χ^2_{ZZ}, high M_X $\ell\ell\ell\ell$ signal regions. The statistical uncertainty on the normalization is the dominant source of uncertainty for the four-lepton non-resonant background prediction.

As one test of the independence of the non-resonant predictions to the number of selected/anti-selected leptons, Table VI shows the parameters and yield predictions obtained by fitting γ for each sample independently of the others. All of the yield predictions are consistent with each other within the statistical uncertainty.

The sideband data fit for the $\ell\ell jj$ non-resonant background estimates consist of events containing a dilepton pair with $\chi^2_Z < 25$ and a dijet pair with either $40 < M_{jj} < 65\,\mathrm{GeV}/c^2$ or

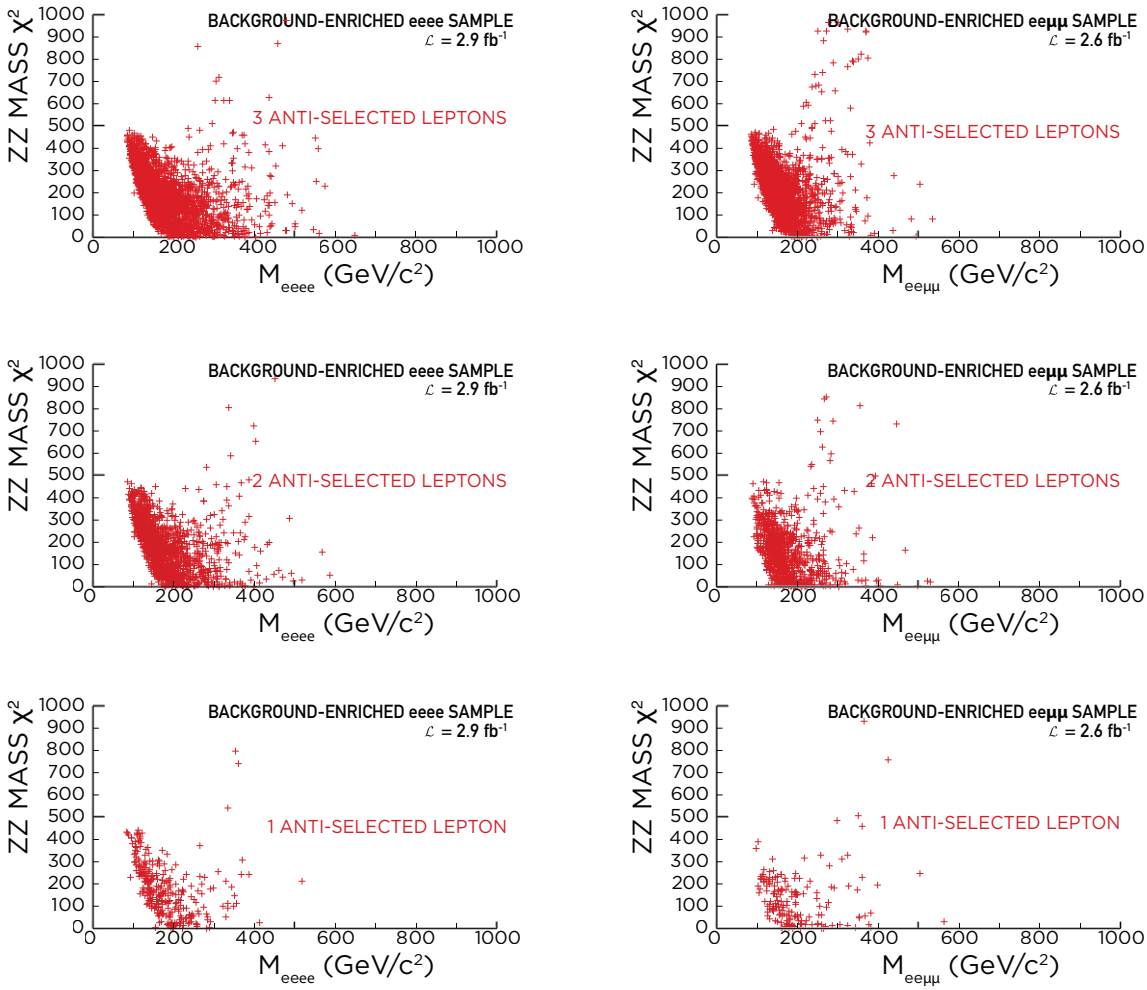

FIG. 5: χ^2_{ZZ} vs. M_X distributions for the four-electron and electron-triggered two-electron two-muon sideband samples with 1, 2, and 3 anti-selected leptons.

$120 < M_{jj} < 200\,\mathrm{GeV}/c^2$. The M_{jj} spectrum near the Z pole mass is exponentially falling before imposing any requirement on M_X but linear for events with $M_X > 300\,\mathrm{GeV}/c^2$, where the effect of the four-body mass cut is to sculpt a peak in the dijet mass at $M_{jj} \gg 200\,\mathrm{GeV}/c^2$ (see Fig. 13). We linearly interpolate the background expectation for $65 < M_{jj} < 120\,\mathrm{GeV}/c^2$ from the lower and higher M_{jj} sideband data. To avoid underestimating the background at very high M_X where these sidebands are empty, we model the population of either sideband vs M_X with an exponential fit to the available data to obtain the numbers used in the interpolation. Fig. 14 shows the numbers of events in the two dijet mass sidebands as a function of the requirement on minimum four-body mass and the exponential fits, which agree well with the data.

As one unbiased test of the prediction of the dijet mass spectrum, we repeat the selection and fit procedure on samples consisting of events containing a trigger lepton plus an anti-selected lepton and at least two jets. Comparison of the fit predictions against these $65 < M_{jj} < 120\,\mathrm{GeV}/c^2$ data, which are depleted of signal, show the method performs well (Tables VII and VIII). The disagreement in the lowest M_{eejj} bin for this and other control samples is a result of a slight deviation from an exponential distribution. This residual variation is taken as an extra systematic in the lowest mass bin.

We determine the backgrounds resonant in both Z masses with Monte Carlo models normalized to the cross-sections predicted by MCFM [21].

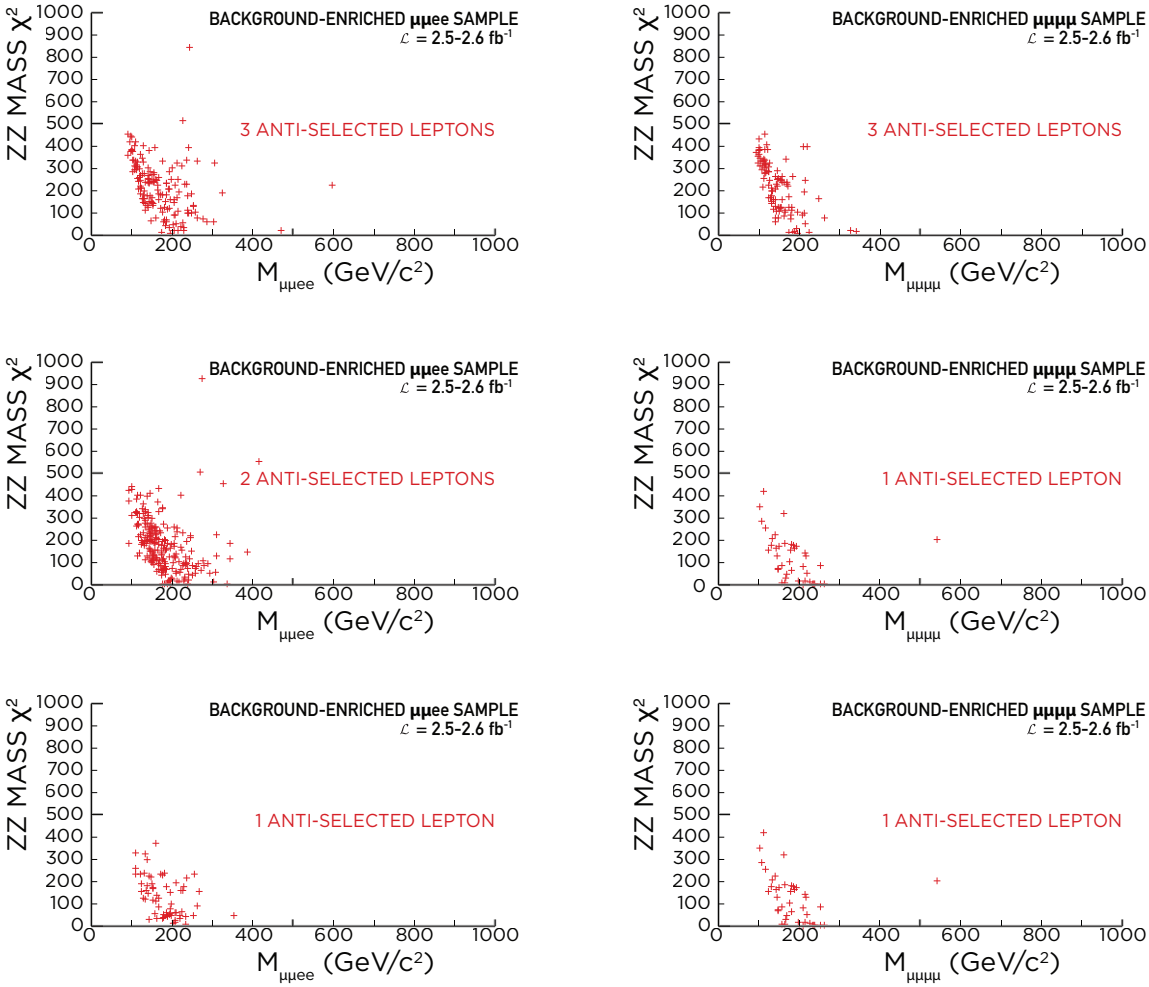

FIG. 6: χ^2_{ZZ} vs. M_X distributions for the muon-triggered two-electron two-muon and four-muon sideband samples with 1, 2, and 3 anti-selected leptons.

TABLE VII: Comparison of dijet mass fit predictions with data for the trigger electron plus anti-selected electron and two-jet channel sample. Shown are the uncertainties on the mean prediction due to fit statistics.

M_{eejj} (GeV/c^2)	Prediction	Observed
350–450	1105 ± 29	941
400–600	488 ± 21	540
500–700	95.6 ± 7.2	115
600–800	18.8 ± 2.0	18
650–950	8.31 ± 1.1	8
750–1050	1.64 ± 0.26	3
800–1200	0.73 ± 0.13	2

TABLE VIII: Comparison of dijet mass fit predictions with data for the trigger muon plus anti-selected muon and two-jet channel sample. Shown are the uncertainties on the mean prediction due to fit statistics.

$M_{\mu\mu jj}$ (GeV/c^2)	Prediction	Observed
350–450	23.7 ± 4.0	22
400–600	9.4 ± 2.2	9
500–700	1.48 ± 0.59	2
600–800	0.23 ± 0.15	1
650–950	0.093 ± 0.072	1
750–1050	0.015 ± 0.017	0
800–1200	0.0059 ± 0.0084	0

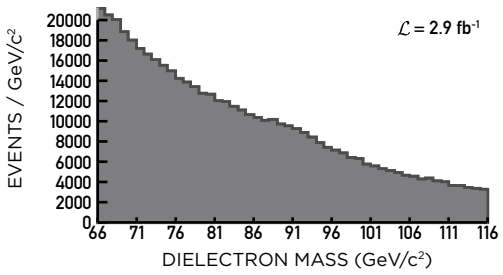

FIG. 7: Invariant mass distribution for pairs of candidates consisting of a trigger electron and an anti-selected electron.

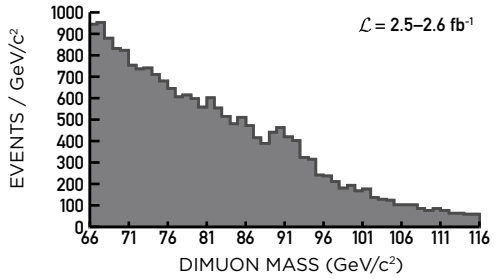

FIG. 8: Invariant mass distribution for pairs of candidates consisting of a trigger muon and an anti-selected muon.

In the $\ell\ell jj$ channels, our dijet mass resolution and analysis selection does not distinguish between the $W^{\pm}Z \to jj\ell\ell$ and $ZZ \to jj\ell\ell$, and so the background from both processes is present.

Tables IX through XIV show the total pre-

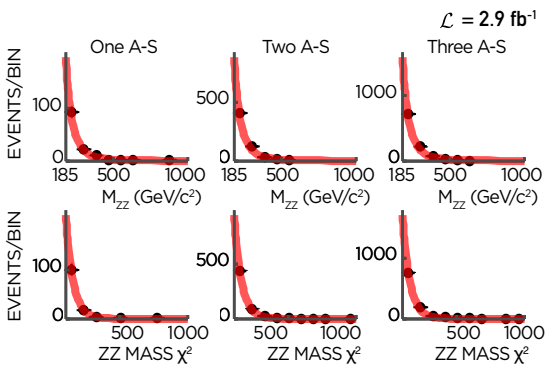

FIG. 9: M_{eeee} and χ^2_{ZZ} for the one-, two-, and three-anti-selected (A-S) four-electron samples, and the results of the simultaneous non-resonant background shape fit to the two- and three-anti-selected electron samples.

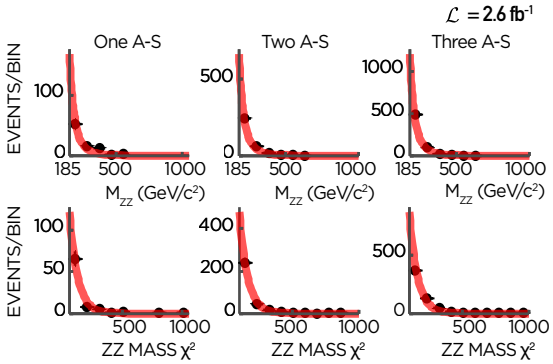

FIG. 10: $M_{ee\mu\mu}$ and χ^2_{ZZ} for the one-, two-, and three-anti-selected (A-S) lepton samples for the electron-triggered two-electron two-muon channel, and the results of the simultaneous non-resonant background shape fit to the two- and three-anti-selected lepton samples.

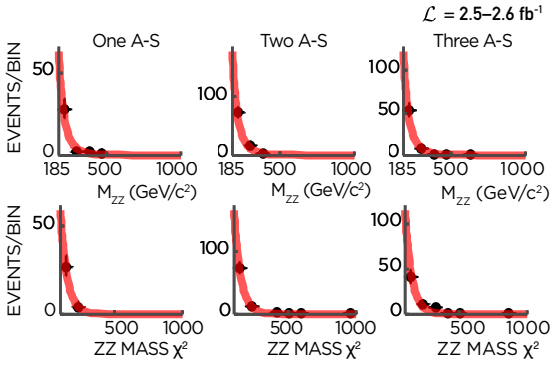

FIG. 11: $M_{\mu\mu ee}$ and χ^2_{ZZ} for the one-, two-, and three-anti-selected (A-S) lepton samples for the muon-triggered two-electron two-muon channel, and the results of the simultaneous non-resonant background shape fit to the two- and three-anti-selected lepton samples.

diction for each analysis channel. At each signal mass, the predictions are integrated over the four-body mass range listed in Table XV. The uncertainties listed for the diboson predictions consist of the error on the MCFM cross-section ($\approx$ 7%), the uncertainty on the luminosity (6%), and the statistical uncertainty due to finite Monte Carlo statistics, which is the dominant uncertainty on the diboson prediction at high four-body mass, though a negligble component of the total background uncertainty. The uncertainties listed for the non-resonant backgrounds consist of the statistical uncertainty from the shape parameters and the normalization uncertainty due to the small number of events in the 185 $<$

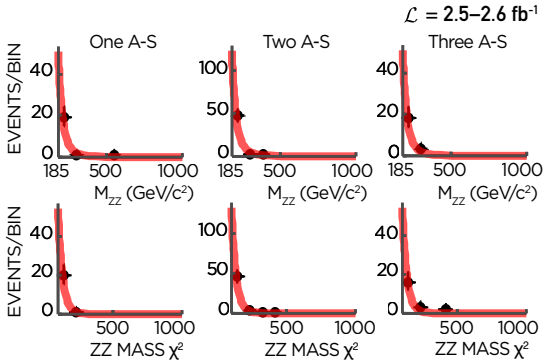

FIG. 12: $M_{\mu\mu\mu\mu}$ and χ^2_{ZZ} for the one-, two-, and three-anti-selected (A-S) four-muon samples, and the results of the simultaneous non-resonant background shape fit to the two- and three-anti-selected muon samples.

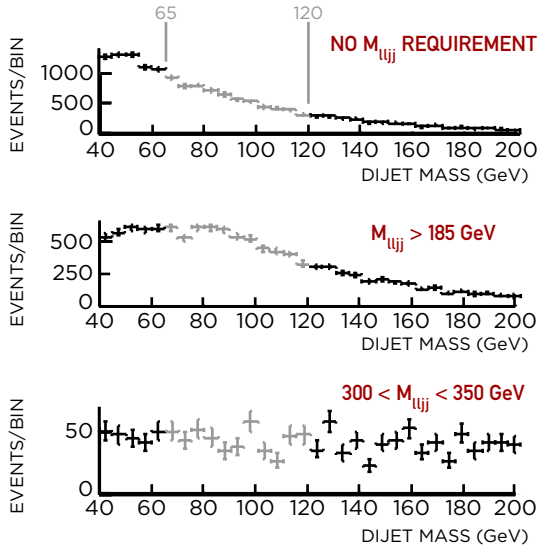

FIG. 13: Dijet mass spectra for two-electron two-jet candidates with $\chi^2_{ee} < 25$ and three M_{eejj} requirements: no requirement, $M_{eejj} > 185\,\mathrm{GeV}/c^2$, and $300 < M_{eejj} < 350\,\mathrm{GeV}/c^2$, beyond which the shape of the dijet mass in the Z region is linear.

$M_X < 300\,\mathrm{GeV}/c^2$ four-lepton control regions. The non-resonant and diboson background systematics are negligible compared to the statistical uncertainty on the total background.

VI. RESULTS

We optimized all selections and estimated all backgrounds before examining the data with

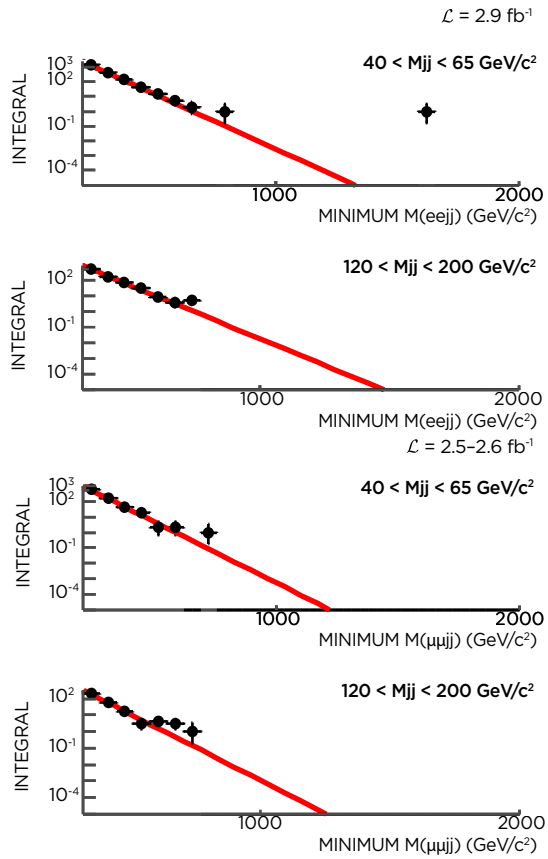

FIG. 14: Number of two-lepton two-jet events with $40 < M_{jj} < 65\,\mathrm{GeV}/c^2$ and $120 < M_{jj} < 200\,\mathrm{GeV}/c^2$ as a function of the minimum M_{lljj} mass requirement, along with the exponential fit to each that is used to interpolate the background prediction for the $65 < M_{jj} < 120\,\mathrm{GeV}/c^2$ region.

TABLE IX: Total $eeee$ backgrounds with $\chi^2{}_{ZZ} < 50$ for each signal mass M_X. The uncertainty includes the ZZ cross-section uncertainty, the luminosity uncertainty, the statistical uncertainty from the simulation, and the statistical uncertainty from the non-resonant background fit.

M_X (GeV/c^2)	SM ZZ	Non-resonant
400	0.22 ± 0.02	1.31 ± 0.44
500	0.086 ± 0.009	0.64 ± 0.29
600	0.045 ± 0.005	0.44 ± 0.18
700	0.020 ± 0.003	0.28 ± 0.20
800	0.007 ± 0.001	0.15 ± 0.12
900	0.005 ± 0.001	0.14 ± 0.11
1000	0.0032 ± 0.0001	0.11 ± 0.10

TABLE X: Total $ee\mu\mu$ backgrounds with ${\chi^2}_{ZZ} < 50$ for each signal mass M_X. The uncertainty includes the ZZ cross-section uncertainty, the luminosity uncertainty, the statistical uncertainty from the simulation, and the statistical uncertainty from the non-resonant background fit.

M_X (GeV/c^2)	SM ZZ	Non-resonant
400	0.19 $\pm$ 0.02	0.33 $\pm$ 0.13
500	0.067 $\pm$ 0.007	0.128 $\pm$ 0.064
600	0.035 $\pm$ 0.004	0.075 $\pm$ 0.047
700	0.014 $\pm$ 0.002	0.041 $\pm$ 0.029
800	0.004 $\pm$ 0.001	0.019 $\pm$ 0.013
900	0.003 $\pm$ 0.001	0.016 $\pm$ 0.013
1000	0.0013 $\pm$ 0.0006	0.012 $\pm$ 0.011

TABLE XI: Total $\mu\mu ee$ backgrounds with ${\chi^2}_{ZZ} < 50$ for each signal mass M_X. The uncertainty includes the ZZ cross-section uncertainty, the luminosity uncertainty, the statistical uncertainty from the simulation, and the statistical uncertainty from the non-resonant background fit.

M_X (GeV/c^2)	SM ZZ	Non-resonant
400	0.077 $\pm$ 0.008	0.32 $\pm$ 0.16
500	0.027 $\pm$ 0.003	0.130 $\pm$ 0.077
600	0.014 $\pm$ 0.002	0.078 $\pm$ 0.055
700	0.0065 $\pm$ 0.0010	0.044 $\pm$ 0.034
800	0.0018 $\pm$ 0.0007	0.021 $\pm$ 0.017
900	0.0014 $\pm$ 0.0006	0.018 $\pm$ 0.017
1000	0.0011 $\pm$ 0.0005	0.014 $\pm$ 0.013

$M_{lll} > 300\,\mathrm{GeV}/c^2$ or with a dilepton pair having $\chi^2_Z < 25$ and a dijet pair with $65 < M_{jj} < 120\,\mathrm{GeV}/c^2$. Figs. 15 and 16 show the data in these regions and the combined resonant and non-resonant background predictions for all four-lepton channels and for both dijet channels. In all cases the data agree with the total background prediction and provide no compelling evidence for resonant ZZ production. The highest-mass $\ell\ell\ell\ell$ event (577 GeV/c^2) consists of four muons. For this event, one Z candidate has a mass of $79 \pm 4.2\,\mathrm{GeV}/c^2$ and the other Z candidate has a mass of $400 \pm 170\,\mathrm{GeV}/c^2$. The large mass uncertainty of the second Z comes from a large curvature uncertainty in the measurement of one

TABLE XII: Total $\mu\mu\mu\mu$ backgrounds with ${\chi^2}_{ZZ} < 50$ for each signal mass M_X. The uncertainty includes the ZZ cross-section uncertainty, the luminosity uncertainty, the statistical uncertainty from the simulation, and the statistical uncertainty from the non-resonant background fit.

M_X (GeV/c^2)	SM ZZ	Non-resonant
400	0.090 $\pm$ 0.010	0.21 $\pm$ 0.11
500	0.036 $\pm$ 0.005	0.063 $\pm$ 0.040
600	0.018 $\pm$ 0.002	0.031 $\pm$ 0.023
700	0.0082 $\pm$ 0.0015	0.015 $\pm$ 0.013
800	0.0018 $\pm$ 0.0007	0.0056 $\pm$ 0.0049
900	0.00011 $\pm$ 0.00005	0.0046 $\pm$ 0.0042
1000	0.0009 $\pm$ 0.0005	0.0031 $\pm$ 0.0030

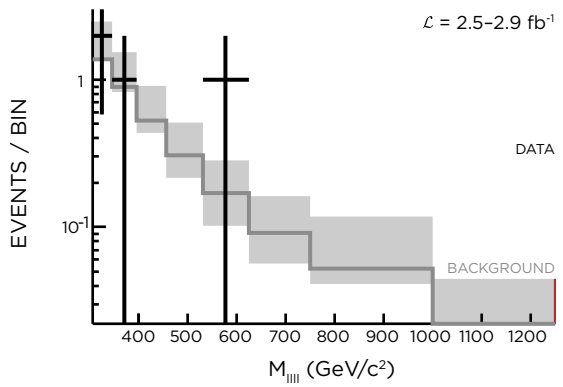

FIG. 15: Prediction and data for all four-lepton channels combined. The background prediction for each bin consists of the integral of the non-resonant background functions and diboson Monte Carlo determined in Section V. The background predictions agree with the data.

$p_T = 290\,\mathrm{GeV}/c$ muon with few COT hits. The highest-mass $\ell\ell jj$ event (868 GeV/c^2) has $M_{ee} = 96.5 \pm 1.3\,\mathrm{GeV}/c^2$ and $M_{jj} = 77.8 \pm 6.5\,\mathrm{GeV}/c^2$.

Absent evidence of a signal, we communicate our sensitivity to $X \to ZZ$ processes by setting limits with an acceptance from a widely-available HERWIG Monte Carlo process [22], the spin-2 Kaluza-Klein graviton. The total acceptance times efficiency for this process varies between roughly 40-50% for a given four-lepton channel and between 20-40% for a given dijet channel (Fig. 17). At higher masses, the fraction of Z decays increases in which the angular

TABLE XIII: Total $eejj$ backgrounds with $65 < M_{jj} < 120\,\mathrm{GeV}/c^2$ for each signal mass M_X. The uncertainty includes diboson cross-section uncertainties, the uncertainty on the luminosity, the statistical uncertainty from the simulation, and the uncertainties from the non-resonant background fits.

M_X (GeV/c^2)	SM ZZ	SM $W^{\pm}Z$	Non-resonant
400	5.72 ± 0.97	9.4 ± 1.1	483 ± 18
500	2.43 ± 0.58	3.25 ± 0.46	128.0 ± 8.2
600	0.99 ± 0.36	1.10 ± 0.22	47.4 ± 4.1
700	0.19 ± 0.18	0.60 ± 0.16	14.9 ± 1.7
800	$0^{+0.11}$	0.158 ± 0.083	2.86 ± 0.46
900	$0^{+0.11}$	0.095 ± 0.067	1.75 ± 0.31
1000	$0^{+0.11}$	$0^{+0.067}$	0.77 ± 0.16

TABLE XIV: Total $\mu\mu jj$ backgrounds with $65 < M_{jj} < 120\,\mathrm{GeV}/c^2$ for each signal mass M_X. The uncertainty includes diboson cross-section uncertainties, the uncertainty on the luminosity, the statistical uncertainty from the simulation, and the uncertainties from the non-resonant background fits.

M_X (GeV/c^2)	SM ZZ	SM $W^{\pm}Z$	Non-resonant
400	2.90 ± 0.57	6.04 ± 0.73	162 ± 11
500	1.30 ± 0.38	2.06 ± 0.32	37.7 ± 4.4
600	0.57 ± 0.26	0.73 ± 0.17	12.6 ± 2.0
700	0.26 ± 0.19	0.229 ± 0.93	3.53 ± 0.72
800	0.09 ± 0.13	0.023 ± 0.040	0.57 ± 0.16
900	$0^{+0.10}$	$0^{+0.032}$	0.33 ± 0.10
1000	$0^{+0.10}$	$0^{+0.032}$	0.133 ± 0.045

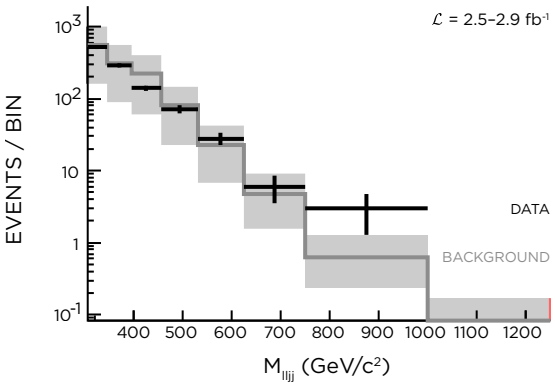

FIG. 16: Prediction and data for both $\ell\ell jj$ channels combined. The background prediction for each bin consists of the integral of the non-resonant background functions and diboson Monte Carlo determined in Section V. The background predictions agree with the data.

separation between products is too small for the calorimeter to resolve. This lowers the acceptances for the dijet modes and, to a lesser extent, the electron modes.

The combined effect of the lepton reconstruction and identification improvements on graviton signal is demonstrated in Figs. 18 and 19 for the four-electron and four-muon channels. We compute data yields and estimates of signal and background by integrating the Monte Carlo predictions and fitted non-resonant background shapes over a set of overlapping, variable-width bins for signal masses from 400 GeV/c^2 to 1 TeV/c^2 (Table XV). Each signal bin width is chosen to be large enough to fully contain the four-body mass distribution expected for an intrinsically narrow signal and the broadening from systematic effects.

We calculate 95%-credibility upper limits as a function of signal mass using a six-channel product of Bayesian likelihoods and a uniform prior for the (non-negative) $X \to ZZ$ cross-section.

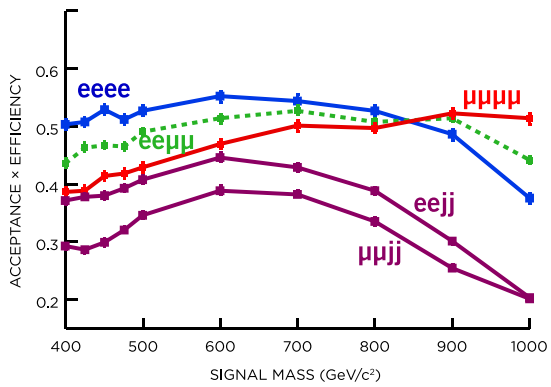

FIG. 17: Products of acceptance times efficiency for each of the graviton analysis channels and their dependence on graviton mass. These do not include ZZ branching ratios, which for each $ZZ \to \ell\ell jj$ mode are approximately 40 times the branching ratios for $ZZ \to eeee$ or $ZZ \to \mu\mu\mu\mu$. The $ee\mu\mu$ and $\mu\mu ee$ acceptances have been summed.

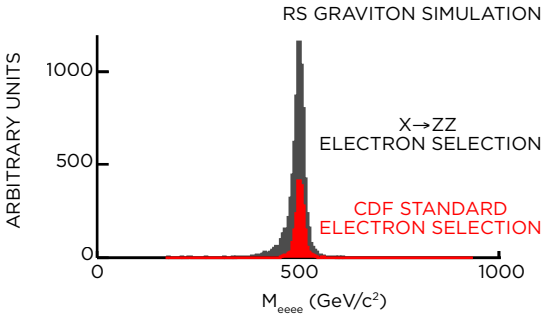

FIG. 18: Four-electron yield comparison for a 500 GeV/c^2 graviton between (lower histogram) the CDF standard electron selection criteria and (upper histogram) the criteria employed in the present analysis.

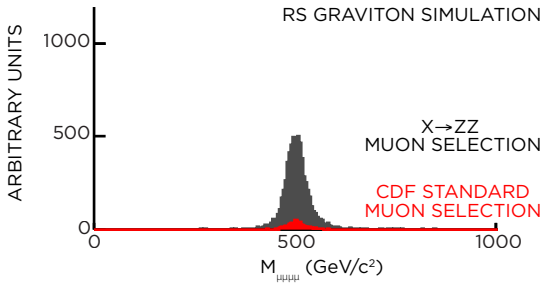

FIG. 19: Four-muon yield comparison for a 500 GeV/c^2 graviton between (lower histogram) a CDF standard muon selection criteria and (upper histogram) the criteria employed in the present analysis.

TABLE XV: Signal binning used for limit-setting.

Signal Mass (GeV/c^2)	Bin Half Width (GeV/c^2)
400 ±	70
500 ±	90
600 ±	130
700 ±	160
800 ±	160
900 ±	230
1000 ±	280

We use marginalized truncated-Gaussian nuisance parameters for the luminosity, background predictions, and signal efficiencies, and we account for systematic uncertainties correlated amongst the six channels when appropriate. As discussed earlier, we assign a 20% uncorrelated uncertainty to the total acceptance × efficiency for each channel to account for the observed time-dependent variation in the Drell-Yan $\mu\mu$ cross-section, conservatively covering the sum of individual systematic uncertainties such as signal acceptance uncertainties in order to simplify the combination. Studies of the individual uncertainties indicate the largest contribution after the uncertainty due to the $Z \to \mu\mu$ cross section variation is the 5.9% uncertainty on the luminosity. In addition to the observed limit, we compute expected limits from 10,000 pseudo-experiments at each candidate X mass. Fig. 20 shows the resultant limits along with the $k/M_p = 0.1$ Randall-Sundrum (RS1) graviton cross-section from HERWIG. The present search improves the $\mathcal{O}(4$ pb) limit of the earlier $eeee$ search [8] by an order of magnitude.

VII. CONCLUSIONS

We have reported on an improved search for a massive resonance decaying to ZZ via the $eeee$, $ee\mu\mu$, $\mu\mu\mu\mu$, $eejj$, and $\mu\mu jj$ channels. We find that the four-body invariant mass spectrum above 300 GeV/c^2 is consistent with background estimates derived from sideband data samples and electroweak Monte Carlo models. To quantify our sensitivity, we set limits using the acceptance for a Randall-Sundrum graviton model that are 7–20 times stronger than the previously published direct limits on resonant ZZ produc-

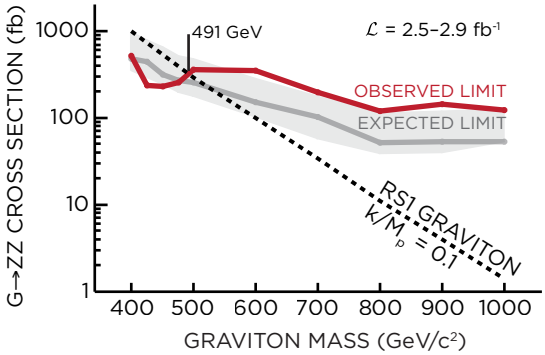

FIG. 20: 95%-credibility cross-section limit assuming acceptance for a massive graviton along with the limit and 68% variation expected for the background-only hypothesis.

tion.

Acknowledgments

We thank the Fermilab staff and the technical staffs of the participating institutions for their vital contributions. This work was supported by the U.S. Department of Energy and National Science Foundation; the Italian Istituto Nazionale di Fisica Nucleare; the Ministry of Education, Culture, Sports, Science and Technology of Japan; the Natural Sciences and Engineering Research Council of Canada; the National Science Council of the Republic of China; the Swiss National Science Foundation; the A.P. Sloan Foundation; the Bundesministerium für Bildung und Forschung, Germany; the Korean World Class University Program, the National Research Foundation of Korea; the Science and Technology Facilities Council and the Royal Society, UK; the Institut National de Physique Nucleaire et Physique des Particules/CNRS; the Russian Foundation for Basic Research; the Ministerio de Ciencia e Innovación, and Programa Consolider-Ingenio 2010, Spain; the Slovak R&D Agency; and the Academy of Finland.

Appendix

The standard CDF reconstruction software uses two main approaches to reconstruct tracks. High quality central tracking ($|\eta| < 1$) starts in the COT and assembles piecewise segments of up to 12 hits in each superlayer, fits them, and groups them into tracks to which any available silicon hits are then attached in an outside-in search. Afterward, "silicon standalone" tracking starts with all possible combinations of three unused silicon hits, searches the remaining silicon layers, and projects successful tracks into the COT to attach any compatible hits in order to improve the track momentum resolution and lower the fake rate.

The combination of these approaches results in low efficiency in the $1 < |\eta| < 2$ region. Tracks originating from $z = 0$ with $|\eta| < 1.7$ will leave traces of their passage in the lowest-radii superlayers of the COT. Though very efficient when full COT coverage is available, for $|\eta| > 1$ the central tracking algorithms lose efficiency nearly linearly with $|\eta|$ reaching zero efficiency at about $|\eta| = 1.6$. The silicon fully covers $|\eta| < 1.8$ to compensate for the falling COT efficiency, but the existing silicon-driven tracking algorithms reconstruct tracks with low efficiency and produce low-quality or spurious tracks with poor pointing resolution into the COT. Thus the COT information for forward tracks is rarely exploited.

This analysis employs a thorough revision of the forward and central tracking algorithms in order to reconstruct tracks with better efficiency and resolution, including a new "Backward" algorithm that makes full use of the partial COT coverage. The Backward algorithm, illustrated in Fig. 21 for a simple case, starts by searching the COT for hits unused by the central COT algorithm and constructing segments in one of the inner axial superlayers consisting of no more than 12 hits. At this stage, the position measurements contain a drift sign ambiguity and important drift time corrections, such as large time of flight and sense wire signal propagation times, are unknown and cannot be approximated by the constant corrections assumed for the central segment pattern recognition. The Backward algorithm solves this problem with a variant of the central segment pattern recognition that resolves the drift sign ambiguity and drift time corrections during the search and is optimized for tracking in the low radius, high hit density inner superlayers and near the COT endplates. Once unused COT hit segments are found consistent with a forward track, the algorithm then fits the segments with a beamline constraint to obtain five-parameter helices that intersect the z position of the highest sum p_{T} z vertex identified using central algorithm tracks. In most cases, the fits do not conclusively identify stereo COT

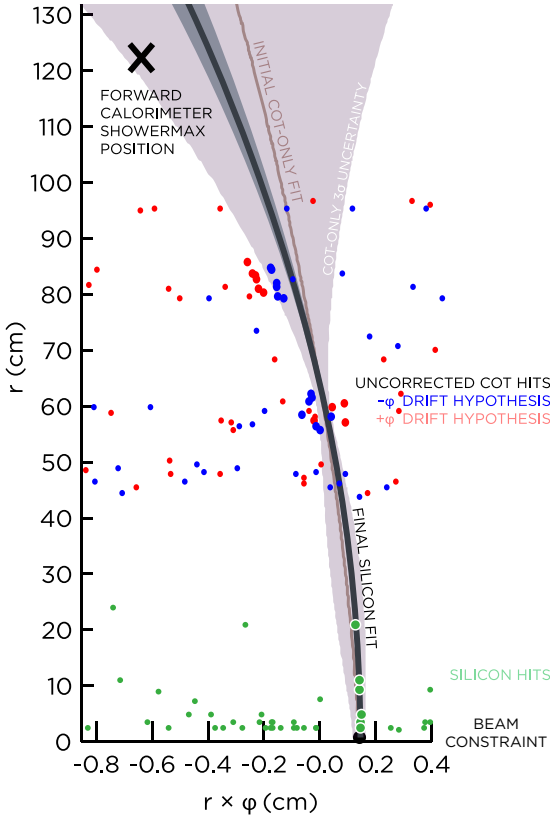

FIG. 21: A simple example of the Backward tracking algorithm in low luminosity data. In a stretched and rotated $r-\phi$ view of the relevant section of the tracking volume, COT pulses in a single 12-layer axial superlayer indicating two possible hit locations corresponding to $-\phi$ and $+\phi$ drift are processed to identify trajectory segments and fitted to obtain drift time corrections and an initial trajectory with large uncertainties. An iterative Kalman filter search through possible η values for silicon charge clusters consistent with the initial trajectory produces a tree of track possibilities, from which the single best candidate, shown with a projection of the final 3σ uncertainties, is chosen. Also shown is an independent measurement from the forward calorimeter shower maximum scintillator.

measurements in the innermost stereo superlayer, and so multiple helices are obtained corresponding to trajectories through each possible combination of silicon module and polar angle. Drift time corrections are recomputed for each case.

After obtaining initial helix fits, including estimates of the helix uncertainties and correlations obtained from the small number of COT hits, the algorithm begins an outside-in silicon hit search that uses a Kalman filter to correct for energy loss and multiple scattering in the tracker material. After each search completes, quality criteria based on hit pattern, multiple usage, charge deposition, and module operational status are applied to the successful hypotheses, and all surviving hypotheses except those with the most hits are discarded. Finally, the COT is searched for any remaining information, including stereo measurements in inner superlayers.

The Backward algorithm has been validated on a variety of samples, with emphasis on large samples of $Z \to ee$ and $Z \to \mu\mu$ simulation and data. Fig. 22 shows the improvement in $Z \to \mu\mu$ yield in muon-triggered data involving higher-quality forward tracks with COT hits in a subset of the data, demonstrating the increase in muon acceptance due to the new software. The lower curve represents the dimuon mass spectrum for the combination of a trigger muon tracked with the central algorithm and a forward muon tracked in the combination of the COT and the silicon detectors with the silicon-driven algorithm in the standard software. The upper curve shows the same spectrum in the new software, where the Backward algorithm has largely superseded the other silicon-driven algorithm. With a modest increase in background, the peak yield has improved by about 260%, corresponding to an approximately 10% increase in the total $Z \to \mu\mu$ yield over the entire detector. The distributions of all forward muon identification variables are qualitatively the same as those of muons found with the central COT-driven algorithm, indicating that we have selected a sample of forward muons with purity comparable to the central muons.

[1] T. Aaltonen *et al.* (CDF Collaboration), Phys. Rev. Lett. **100** 201801 (2008).
[2] V. M. Abazov *et al.* (D0 Collaboration), Phys. Rev. Lett. **101** 171803 (2008).
[3] ALEPH Collaboration, Phys. Lett. B **469** 287 (1999).
[4] DELPHI Collaboration, Eur. Phys. J. C **30** 447 (2003).
[5] L3 Collaboration, Phys. Lett. B **572** 133 (2003).
[6] OPAL Collaboration, Eur. Phys. J. C **32** 303

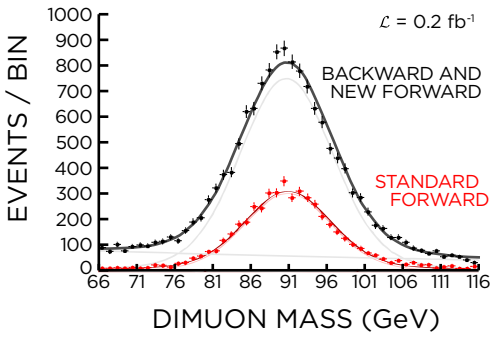

FIG. 22: $Z \to \mu\mu$ yield and background comparison in $0.2\,\mathrm{fb}^{-1}$ of data for candidates combining a trigger muon with another muon reconstructed by any dedicated forward tracking algorithm for (lower curve) the standard CDF reconstruction and (upper curve) the reconstruction used for the present analysis. The gray curves indicate the shapes and normalization of the signal (Breit-Wigner distribution convolved with a Gaussian resolution function) and background (exponential distribution) components used in the fit. In both cases, attached COT hits and the muon identification criteria listed in Table III are applied.

(2003).
[7] H. Davoudiasl, J. L. Hewett, and T. G. Rizzo, Phys. Rev. Lett. **84** 2080 (2000).
[8] T. Aaltonen *et al.* (CDF Collaboration), Phys. Rev. D **78** 12008 (2008).
[9] L. Randall and R. Sundrum, Phys. Rev. Lett. **83** 4690 (1999).
[10] L. Randall and R. Sundrum, Phys. Rev. Lett. **83** 3370 (1999).
[11] K. Agashe, H. Davoudiasl, G. Perez, and A. Soni, Phys. Rev. D **76** 36006 (2007).
[12] L. Fitzpatrick, J. Kaplan, L. Randall, and L.-T. Wang, J. High Energy Phys. **09** 013 (2007).
[13] A. Abulencia *et al.* (CDF Collaboration), J. Phys. G **34** 2457 (2007).
[14] A. Sill *et al.*, Nucl. Instrum. Methods A **447** 1 (2000).
[15] T. Affolder *et al.*, Nucl. Instrum. Methods A **526** 249 (2004).
[16] L. Balka *et al.*, Nucl. Instrum. Methods A **267** 272 (1988).
[17] D. Acosta *et al.*, Nucl. Instrum. Methods A **461** 540 (2001).
[18] F. Abe *et al.* (CDF Collaboration), Phys. Rev. D **44** 1 29 (1991).
[19] F. Abe *et al.* (CDF Collaboration), Phys. Rev. D **45** 5 1448 (1992).
[20] A. Bhatti *et al.*, Nucl. Instrum. Methods A **566** 375 (2006).
[21] J. M. Campbell and R. K. Ellis, Phys. Rev. D **60** 113006 (1999).
[22] G. Corcella *et al.*, JHEP **01** 010 (2001).